

A STUDY OF GPS MEASUREMENT ERRORS DUE TO NOISE AND MULTIPATH INTERFERENCE FOR CGADS

Final Report

Submitted to NASA Goddard Spaceflight Center

Scientific Officer - Seymor Kant, Code 701

Principal Investigators - Penina Axelrad, Peter F. MacDoran

Graduate Student - Christopher J. Comp

Colorado Center for Astrodynamics Research
University of Colorado, CB 431
Boulder, CO 80309

January 31, 1996

NASA Award: NCC 5-67, C.U. Account: 153-7552

ABSTRACT

This report describes a study performed by the Colorado Center for Astrodynamics Research (CCAR) on GPS measurement errors in the Codeless GPS Attitude Determination System (CGADS) due to noise and multipath interference. Preliminary simulation models of the CGADS receiver and orbital multipath are described. The standard FFT algorithm for processing the codeless data is described and two alternative algorithms - an auto-regressive/least squares (AR-LS) method, and a combined adaptive notch filter/least squares (ANF-ALS) method, are also presented. Effects of system noise, quantization, baseband frequency selection, and Doppler rates on the accuracy of phase estimates with each of the processing methods are shown. Typical electrical phase errors for the AR-LS method are 0.2 degrees, compared to 0.3 and 0.5 degrees for the FFT and ANF-ALS algorithms, respectively. Doppler rate was found to have the largest effect on the performance.

1.0 INTRODUCTION

The objective of this study was to quantify the accuracy achievable with the codeless GPS attitude determination system (CGADS) including the effects of noise and multipath. Our initial focus was on receiver and multipath modeling. The expectation was that experimental data from a prototype receiver would become available during the course of the project and that this information could be incorporated into the simulation models. Because of delays in receiver development, the emphasis shifted to an evaluation of alternative data processing techniques which could be used for improved frequency and phase estimation.

The following Section provides both the detailed receiver simulation and a simplified version used for data processing algorithm testing. Section 3 details the preliminary multipath simulation and results. Sections 4-7 describe the basic FFT algorithm and two alternative approaches for processing the baseband signal inside the CGADS receiver. The first approach is based on an autoregressive signal model and the second combines adaptive notch filter and least squares algorithm. Section 8 presents results for all algorithms in terms of frequency and electrical phase errors. Effects of thermal noise, baseband frequency, quantization, and Doppler rate are considered. The last section provides a summary and recommendations.

2.0 SIMULATION DESCRIPTIONS

Section 2.1 describes the computer simulation that models multipath and its effect in the CGADS receiver. The simulation was performed for a earth pointing spacecraft in a circular orbit at an altitude of 500 kilometers. A single antenna, reflector, and GPS signal were used to produce multipath phase error values. The phase error was computed using two methods for comparison. One method computed the phase using the peaks in the FFT spectrum of the in-phase and quadrature components of the squared signal. The other computed the phase using an analytical formula.

Signal processing techniques other than the FFT were also investigated. Section 2.2 details the simplified signal model devised to easily accomplish this task. A multipath-free 2-antenna platform, remaining stationary over the time of analysis, was assumed. A batch

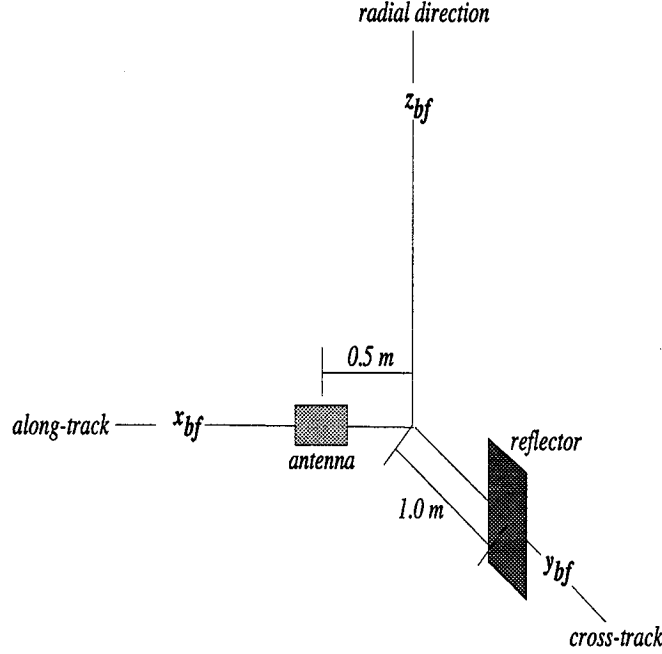


Figure 1: Illustration of antenna and reflector locations in the body-fixed frame of the simulated spacecraft.

Auto-Regressive and an adaptive filter algorithm were used to compute the frequency and phase of the simulated GPS.

2.1 MULTIPATH SIMULATION

The simulated platform is an earth pointing satellite traveling in a 500 kilometer altitude circular orbit inclined at 23.5 degrees. A nominal GPS orbit at 20,000 kilometers altitude and 55 degrees inclination is also simulated. The sketch in Figure 1 illustrates the axes of reference for the spacecraft, and the antenna and reflector locations. Since the spacecraft is earth pointing, the body-fixed frame remains aligned with the orbit local, which has its x , y , and z , axes aligned with the along-track, cross-track, and radial directions, respectively. A single GPS antenna is located at $(x,y,z)=(0.5,0,0)$ in the body-fixed frame. A reflector is positioned at $(0,1,0)$ in the body-fixed frame. The associated reflectivity coefficients used were $\alpha=0.1, 0.2$, and 0.5 . The reflector represents a worst case scenario, in which the GPS signal is always reflected towards the antenna regardless of the incident ray geometry. A more realistic model would include a limited surface, for which the ray path would not necessarily be reflected upon the antenna. The antenna has visibility in the upper half plane of the body frame (*i.e.* the positive z_{bf} direction). The simulation duration is chosen such that the GPS satellite elevation, as seen by the antenna, traverses from 0 through 90 and back to 0 degrees. As the orbiting platform passes beneath the GPS satellite, knowledge of the line-of-sight vector is used to compute the phase of the multipath signal relative to the direct. The determination of the measured phase error depends on the type of receiver simulated (codeless or code-correlating), and will be described in Sections 2.1.1 and 2.1.2.

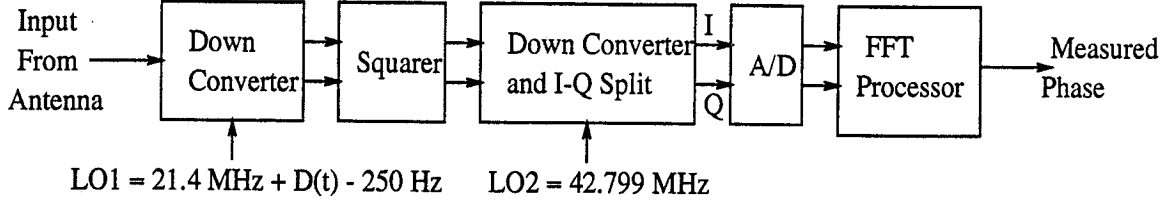


Figure 2: Functional diagram showing basic CGADS receiver functions.

2.1.1 CODELESS RECEIVER

The multipath in the codeless receiver is simulated for the spacecraft scenario described in Section 2.1. A multipath corrupted GPS signal entering the receiver via an isotropic antenna passes through a downconverter. The local oscillator (LO) frequency at this first stage is $21.4 \text{ MHz} + D(t) - 250 \text{ Hz}$. The $D(t)$ is used to compensate for the Doppler at the L1 frequency (1575.42 MHz) at regular intervals. The signal then passes through a squaring device, and an in-phase and quadrature splitter incorporating a second downconverter. The LO frequency for the second downconversion stage is 42.799 MHz. The signal flow just described is shown by the functional diagram in Figure 2. The final in-phase (I) and quadrature (Q) signals are at a baseband frequency of $\omega_b = 500 \text{ Hz}$, which is a consequence of squaring the 250 Hz offset from the first downconverter. Expressions were derived for the I and Q signals, expressed as S_I and S_Q below:

$$S_I = \frac{A^2}{16} [\cos(\omega_b t) + 2\alpha \cos(\phi + \omega_b t) + \alpha^2 \cos(2\phi + \omega_b t)] \quad (1)$$

$$S_Q = -\frac{A^2}{16} [\sin(\omega_b t) + 2\alpha \sin(\phi + \omega_b t) + \alpha^2 \sin(2\phi + \omega_b t)] \quad (2)$$

where A is the amplitude of the direct GPS signal, α the relative amplitude of the multipath (equal to the reflectivity), and ϕ the relative phase of the multipath compared to the direct. Equations 1 and 2 have been corrected for errors which were present in the original expressions that were provided in the memorandum sent July 15, 1994.

The I and Q signals pass through an analog to digital converter which samples at 2560 Hz over a time span of 0.1 second, producing 256 samples for FFT processing. The baseband frequency is recentered to 500 Hz at the start of each 0.1 second period by compensating for the Doppler in the 1st LO. The sampled I and Q sequences are packed into the real and imaginary components of a complex vector, from which a complex FFT is computed. The combination of sampling frequency and duration produces an FFT resolution bandwidth of 10 Hz. The peak magnitude in the FFT sequence is identified, and the phase is computed by taking the inverse tangent of the imaginary over the real part of that FFT value:

$$\begin{aligned} \theta &= \frac{1}{2} \tan^{-1} \left[\frac{\text{imag}(FFT(I + iQ))}{\text{real}(FFT(I + iQ))} \right] \\ &= \frac{1}{2} \tan^{-1} \left[\frac{FFT(Q)}{FFT(I)} \right] \end{aligned} \quad (3)$$

Using the imaginary and real parts of the complex FFT is equivalent to the real-valued FFT of the Q and I signals, respectively. In hardware, it is more efficient to perform a single

complex FFT than two real FFTs. This is how it is done in CGADS, and the simulation conforms to this method.

The phase is calculated for signals with and without multipath according to Equation 3. The two are then differenced, producing the phase error due to multipath:

$$\delta\theta = \theta_{MP} - \theta \quad (4)$$

This result is compared with the value obtained from an analytical expression for the multipath phase error for a single multipath signal. Expand the trigonometric terms in Equation 1, and collect those that contain $\sin(\omega_b)$ and $\cos(\omega_b)$. The phase error is equal to the inverse tangent of the $\sin(\omega_b)$ terms over the $\cos(\omega_b)$ terms:

$$\delta\theta_{analytical} = \frac{1}{2} \tan^{-1} \left[\frac{-2\alpha \sin(\phi) - \alpha^2 \sin(2\phi)}{1 + 2\alpha \cos(\phi) + \alpha^2 \cos(2\phi)} \right] \quad (5)$$

2.1.2 CODE-CORRELATING RECEIVER

The multipath in a code-correlating receiver is also simulated for the spacecraft scenario described in Section 2.1. The typical receiver downconverts the received signal to an IF frequency, and digitally samples to produce I and Q components. It then aligns the received signal with a locally generated replica using a delay lock loop (DLL). The output of the punctual correlator is the recovered carrier signal. This recovered IF signal, consisting of both direct and multipath components, serves as one input to a phase-lock loop (PLL). The other input to the PLL is a local replica of the carrier generated by an NCO. In a standard receiver, the output frequency of the NCO is controlled so as to make the local signal align with the received signal. Thus, when the PLL first achieves frequency lock between the local and incoming signals, a phase comparator can measure the fractional phase difference of the two signals - this is the phase offset. Thereafter, subsequent commands to the NCO essentially keep track of changes in this phase difference.

Assuming perfect code-correlation, an expression for the recovered IF carrier, contaminated by a single multipath signal, is given as:

$$S_{if} = A [(1 + \alpha \cos(\phi)) \cos(\omega_{if}t) - \alpha \sin(\phi) \sin(\omega_{if}t)] \quad (6)$$

where A is the amplitude of the direct signal, α the relative amplitude of the multipath, and ϕ the relative phase of the multipath. The IF frequency ω_{if} is basically the Doppler frequency. The multipath phase error in the carrier signal is the inverse tangent of the terms containing $\sin(\omega_{if})$ over those containing $\cos(\omega_{if})$:

$$\delta\theta = \tan^{-1} \left[\frac{-\alpha \sin(\phi)}{1 + \alpha \cos(\phi)} \right] \quad (7)$$

2.2 SIMULATION FOR DATA PROCESSING COMPARISONS

Signal processing algorithms for computing the frequency and phase of the GPS carrier signal are to be studied. The following simplified signal model was used to compare algorithm performance for a single batch of 256 data samples. Keep in mind that for this study we do not include effects of two GPS signals present within the antenna field of view.

The true phase of the baseband signal received from antenna A is given by:

$$\phi_A = \phi_0 + 2\pi \left((f_b + f_{Doppler_0})t + 0.5\dot{f}_{Doppler}t^2 \right); \quad (8)$$

where ϕ_0 is the initial phase in radians, f_b is the baseband or center frequency in Hz, $f_{Doppler_0}$ and $\dot{f}_{Doppler}$ are the initial Doppler frequency and its constant rate of change, also in Hz. Using the approximation for thermal phase error based on the assumed SNR:

$$\sigma_\phi = \sqrt{\frac{1}{SNR}} \quad (9)$$

Gaussian random phase error is generated with:

$$\phi_{error} = N(0, \sigma_\phi) \quad (10)$$

During the 0.1 second time of signal analysis the Doppler rate is assumed to be fixed. The in-phase (I) and quadrature (Q) signals are given by:

$$S_{IA} = \cos(\phi_A + \phi_{error}) \quad (11)$$

$$S_{QA} = \sin(\phi_A + \phi_{error} + Q_{delay}) \quad (12)$$

where Q_{delay} represents a delay between the I and Q components. The A/D conversion of the I and Q signals may be modeled by the following scaling and rounding procedure:

$$Sq_{I/QA} = \frac{1}{q} \text{round}(q S_{I/QA}) \quad (13)$$

where q is the quantization level in the A/D (*i.e.* 1sb). A set of expressions similar to Equations 8-13 are used for antenna B . A constant phase difference between A and B , $\Delta\phi$, is introduced.

It is assumed that the vehicle attitude is constant during the 0.1 second measurement batch interval. The implications of this assumption are that the phase difference between the two antennas is constant and the observed Doppler frequencies are the same. In reality, over a 0.1 second interval, a vehicle yaw rate of 0.001 radians/second (comparable to orbit rate) with two antennas A and B separated by 1 meter, could produce a maximum change in the electrical phase difference at 2 L1 of:

$$2\pi \times 0.001 \text{rad/s} \times 0.1 \text{s} \times \frac{1 \text{m}}{0.5 \times 0.1903 \text{m}} = 0.0066 \text{rad} = 0.38 \text{degrees} \quad (14)$$

The Doppler difference at this same yaw rate is negligible with a maximum possible value at 2 L1 of:

$$2 \times (1.57542 \times 10^9 \text{Hz}) \times 0.01 \text{rad/sec} \times \frac{1 \text{m}}{(3 \times 10^8 \text{m/s})} = 0.1 \text{Hz} \quad (15)$$

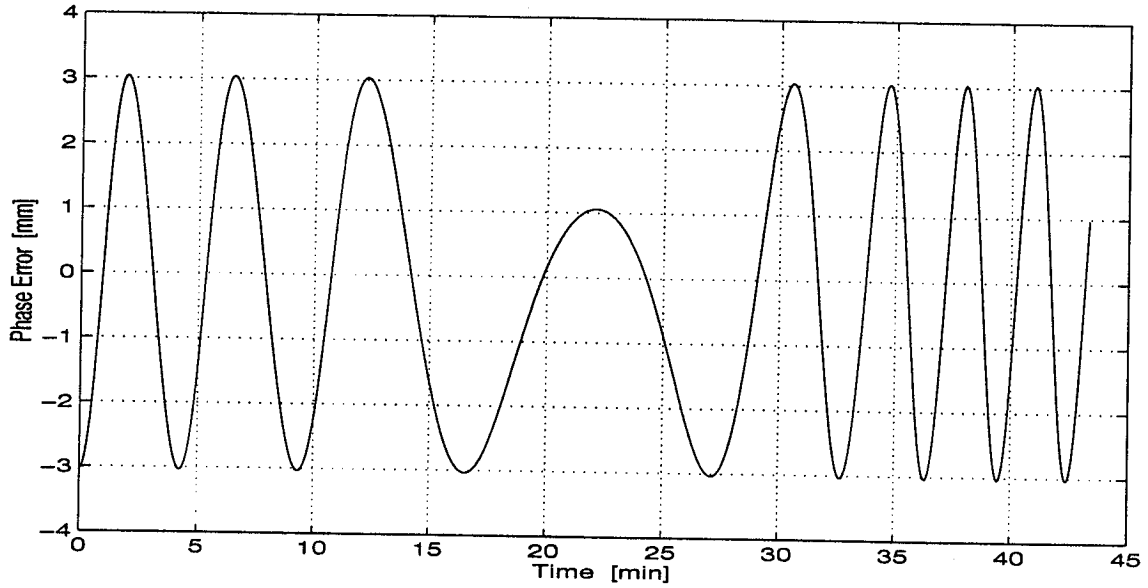


Figure 3: Multipath error computed by the FFT method with $\alpha=0.1$ for the codeless receiver simulation.

Note that the simulations described thus far ignore the Q_{delay} as well as differences in the SNR between the I and Q channels. Furthermore, the simulations model only errors in the electrical signal phase. To convert these errors to attitude, in particular to yaw errors, one must take into account the physical separation of the antennas and the direction to the GPS satellite used. The ideal situation to observe spacecraft yaw, *i.e.* when the electrical phase difference between A and B is most sensitive to changes in yaw, is when both antennas lie in the plane perpendicular to the yaw axis. The line of sight to the GPS satellite is also close to this plane and lies in a direction orthogonal to the line connecting the antennas. In this ideal situation, a yaw error of 1 milliradians would produce a phase change of 3.8 degrees over a 1 meter baseline at 2 L1. Consequently a phase error of 0.2 degrees would produce a corresponding yaw error of 0.052 milliradians.

3.0 MULTIPATH SIMULATION RESULTS

The codeless simulation was executed for the duration described in Section 2.1, which amounted to approximately 45 minutes. The multipath error computed with the FFT method, and for a relative multipath amplitude of $\alpha=0.1$, is provided in Figure 3. The multipath error computed analytically for $\alpha=0.1$ and 0.2 showed differences from the FFT result at the 10^{-3} millimeter level, which are negligible. For the case of $\alpha=0.5$, the FFT method introduced a large bias into the multipath error, which was clearly wrong. After removing the bias, the difference between the analytical and FFT multipath was again negligible. The minute differences are credited to the FFT processing, and it is evident that the multipath introduces considerably more error into the phase measurement than the FFT processing. Aside from numerical issues, the Doppler rate becomes the main problem with the FFT. The changing Doppler during the 0.1 second sampling period tends to smear the peak in the FFT spectrum, and significant errors may arise once it crosses into another

frequency bin (*i.e.* when $d(\text{Doppler})/dt > 100 \text{ Hz/s}$). It is noteworthy then, that at an altitude of 500 kilometers, the present simulation represents an extreme case as far as a Doppler effect on the FFT processing is concerned.

A comparison of the codeless analytical multipath error with the code-correlating multipath error was made. There was some increase in the difference between the two methods for larger alpha. However, they remained on the order of 10^{-5} millimeters and are insignificant for our work. This outcome is intriguing because it highlights the potential to use experience gained in the code-correlating area towards a multipath approach in the codeless receiver. Studying Equations 5 and 7, it is apparent that the differences are caused by the α^2 terms in the codeless expression, which originate from the squaring function.

4.0 FFT ALGORITHM

Using the signal model given in Section 2.2, the I and Q samples for each antenna channel (A and B) are provided by the A/D converter. Nominally a batch of 256 samples is collected at a sample rate of 2560 Hz. The I and Q components are combined into a single complex vector. A 256 point Hanning window is applied to the sample data before it is run through the FFT algorithm. The FFT output consists of a complex number associated with each of the 256 frequency bins, which are spaced 10 Hz apart. The input signal frequency is identified by the bin containing the most power. The input signal phase is determined by the argument of the complex number associated with this bin.

The frequency determined by the FFT method is compared to the “true” frequency, which we will take to mean the average frequency during the 0.1 second interval. This becomes an important distinction when a Doppler rate is introduced. The difference in phase computed for the channel B to channel A signal is compared to the constant phase offset defined in the signal model given in Section 2.2 above.

In essence, this algorithm computes the electrical phase for antenna A by the arc-tangent of the complex FFT value for the frequency bin with the highest power. The same procedure is done for antenna B, and the two phase values are differenced. We did not account for errors made in using a table lookup rather than the actual arc-tangent function. Furthermore we are not sure that this is exactly the same algorithm that Deskin has implemented in their breadboard receiver.

5.0 AUTO-REGRESSIVE (AR) METHOD

The FFT approach, which represents a signal as the sum of sinusoidal signals, can be applied to an arbitrary series of sampled data. On the other hand, the AR method assumes a specific form for the discrete-time process it seeks to model. In particular, a system of order $2p$ is represented by the recursive difference relation:

$$x(n) = - \sum_{k=1}^{2p} a(k)x(n-k) + u(n) \quad (16)$$

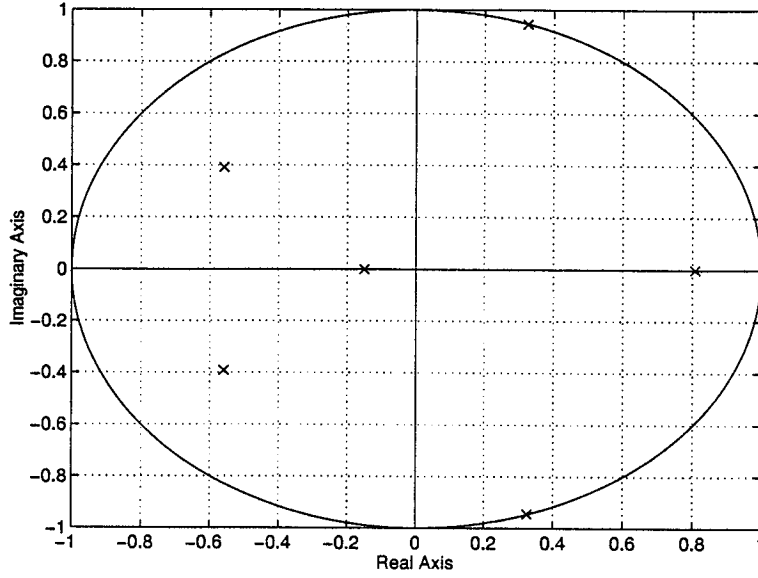


Figure 4: Location of roots of $P(z)$ in AR model with respect to the unit circle, for a signal with baseband frequency of 500 Hz, SNR of 25 dB, and Doppler rate of 100 Hz/s.

Taking the z-transform of the equation above yields the transfer function:

$$\frac{X(z)}{U(z)} = \frac{1}{P(z)} \quad (17)$$

with complex variable

$$z = e^{(\sigma + j\theta)} \quad (18)$$

and denominator polynomial

$$P(z) = 1 + \sum_{k=1}^{2p} a(k)z^{-k} \quad (19)$$

Given a sequence of data, the coefficients $a(k)$ may be estimated using the modified covariance method [2]. Based on these values the roots of $P(z)$ are found. The roots occur in complex conjugate pairs. If an undamped sinusoidal signal is present in the data it will appear as a pair of roots very close to the unit circle (i.e. $\sigma \cong 0$). The angle θ for these roots corresponds to the signal frequency normalized by the sample frequency:

$$\theta = 2\pi f_n, \quad f_n = \frac{f}{f_s} \quad (20)$$

Note that this technique directly estimates the modal frequencies and therefore does not provide estimates which are quantized by discrete frequency bins as does the FFT method.

For the ideal case where there is no noise and the signal is perfectly modeled by a set of p sinusoids, the model order is set to $2p$, and the roots of $P(z)$ will lie exactly on the unit circle at angles of $2\pi f_n$. For the more realistic case where there is noise in the data (or in the system), a higher order model must be used to accommodate the noisy part of the signal. The poles lying closest to the unit circle represent the actual frequencies, and those far from the unit circle represent the noise. If the model order ($2p$) is too low, noise will affect the frequency estimation, and if the order is too high, spurious frequencies may appear.

For the CGADS sampled data considered here we have assumed an AR model order of 6. Figure 4 illustrates the roots of $P(z)$ for the nominal case of a baseband frequency of 500 Hz, SNR of 20 dB, and Doppler rate of 100 Hz/s. The roots corresponding to the frequencies are located on the unit circle, the others are caused by the noise.

Note that the AR algorithm is useful for computing the signal frequency, but it does not provide phase information. However, given the frequency estimate, a least squares solution for the signal phase can be formed. The phase results presented using the AR frequencies and a least squares phase estimate are denoted by AR-LS.

6.0 COMBINED ADAPTIVE NOTCH FILTER AND LEAST SQUARES (ANF-ALS) METHOD

Adaptive spectral parameter estimation such as the adaptive notch filter (ANF) and adaptive least squares (ALS) methods operate on data sequentially. This is the fundamental difference from traditional techniques like the FFT and AR, which instead use batches of data at a time. The end result is a frequency or phase estimate at each measurement time, rather than a single estimate representing an average over the batch time period.

An algorithm combining the IIR ANF and ALS methods was devised based on suggestions in [5]. In essence, the frequencies are first estimated by the ANF. They are subsequently used as truth in the ALS to propagate the state and compute the gain. Based on practical experience, this tends to make the amplitude and argument estimation in the ALS more robust. The combined ANF-ALS algorithm outperforms the individual ones in all areas. The individual ANF and ALS algorithms are described in the following two sections.

6.1 ADAPTIVE NOTCH FILTER (ANF)

The initial motivation for the ANF was to remove quasi-periodic interference from noisy or non-periodic data [4]. A prime example would be a set of measurements corrupted by 60 Hz sinusoidal interference from a power signal. The frequencies of the sinusoidal signals are identified in the process of their removal. For this reason, the ANF eventually became recognized as an excellent tool for spectral parameter estimation.

In the Infinite Impulse Response (IIR) ANF scheme, a notch is produced in the output magnitude response by placing the poles and zeros along the same line radiating out to the unit circle, as illustrated in Figure 5. The angular distance of the line from the real axis is

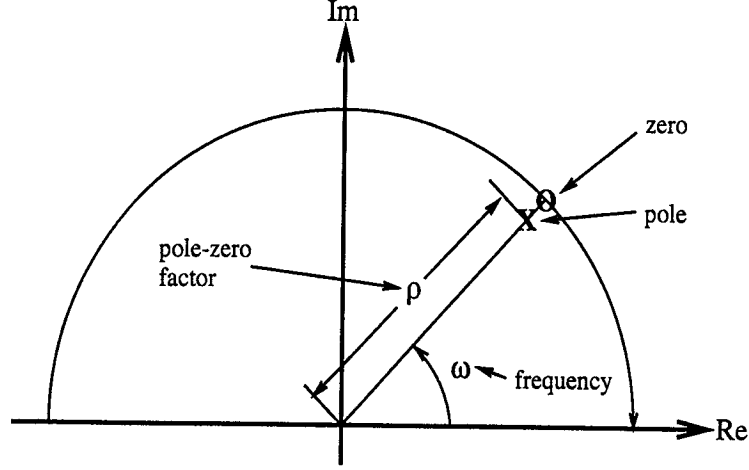


Figure 5: Location of zeros and poles with respect to the unit circle for the IIR adaptive notch filter.

equal to the frequency. For stability, the zeros are constrained to lie on the unit circle. The filter transfer function is given as (c.f. [1,4,5]):

$$H(z^{-1}) = \frac{1 + a_1 z^{-1} + \dots + a_n z^{-n} + \dots + a_1 z^{-2n+1} + z^{-2n}}{1 + \rho a_1 z^{-1} + \dots + \rho^n a_n z^{-n} + \dots + \rho^{2n-1} a_1 z^{-2n+1} + \rho^{2n} z^{-2n}} \quad (21)$$

where the a_i 's are the filter coefficients, and n is the number of desired notches (*i.e.* the number of frequencies to be estimated). The width of the notch, and hence the transition-band, is a function of the proximity of the pole to the zero, signified by the pole-zero contraction factor ρ . The factor must be in the range $0 < \rho < 1$ for a stable filter, $\rho = 1$ forms the ideal notch,

Writing the transfer function as follows:

$$H(z^{-1}) = \frac{A(z^{-1})}{A(\rho z^{-1})} \quad (22)$$

the polynomial $A(z^{-1})$ may be written in either product or summation form:

$$A(z^{-1}) = \prod_{i=0}^n (1 + \alpha_i z^{-1} + z^{-2}) = \sum_{i=0}^{2n} a_i z^{-i}, \quad a_{n+m} = a_{n-m}, \quad m \leq n \quad (23)$$

with closed-form relationships between the a_i and α_i coefficients dependent on n . The frequencies of the sinusoidal signals are directly related to the α_i coefficients by [1]:

$$f_i = \arccos\left(-\frac{\alpha_i}{2}\right) \quad (24)$$

A recursive prediction error algorithm is used to adjust the ANF coefficients in order to remove the quasi-periodic signals. In the process, the frequencies are identified. In

particular, a stochastic Gauss-Newton search method [4] is used to minimize the quadratic criterion:

$$V = \sum_{k=1}^L \epsilon^2(k) \quad (25)$$

where ϵ is the output of the filter, and L the number of data samples.

The IIR ANF requires the use of a second order gradient search, such as the Gauss-Newton method, for two main reasons. The performance surface corresponding to the multi-variable function in Equation 25 may contain local minima, where a global minimum is sought. There are also potential nonlinear instabilities associated with IIR filters in general.

When this algorithm is used to compute the minimum number of filter coefficients, accuracies are within an order of magnitude of the Cramer-Rao bound for large data sets. Moreover, an order of n^2 multiplications are needed, much less than for other ANF algorithms [4]. As input, the algorithm requires the following: sampling frequency, number of frequencies to estimate, convergence parameter and pole-zero contraction factor values, and the data sequence itself. No initial frequency estimates are needed.

6.2 ADAPTIVE LEAST SQUARES (ALS)

The adaptive least squares (ALS) technique begins by modeling the signal under analysis as multiple sinusoids embedded in noise:

$$y(k) = s(k) + \nu(k) = \sum_{i=1}^n A_i(k) \sin(k\omega_i(k) + \phi_i) + \nu(k) \quad (26)$$

where $A_i(k)$ is the amplitude, $\omega_i(k)$ is the frequency, and ϕ_i is the phase offset of the i^{th} sinusoid, and $\nu(k)$ is Gaussian noise, all for the discrete time index $k = 1, \dots, L$. The signal $y(k)$ can be interpreted as noise corrupted measurements of the sinusoids $s(k)$. Define the state space model:

$$s(k) = J^T \theta(k) \quad (27)$$

where the state vector is given as:

$$\theta(k) = \begin{bmatrix} \theta_1(k) \\ \vdots \\ \theta_n(k) \end{bmatrix}, \quad \theta_i(k) = \begin{pmatrix} A_i(k) \sin(k\omega_i(k) + \phi_i) \\ A_i(k) \cos(k\omega_i(k) + \phi_i) \end{pmatrix} \quad (28)$$

and also $J^T = [1 \ 0 \ 1 \ 0 \ \dots \ 1 \ 0]$. Next define the state transition matrix:

$$F(k+1, k) = \begin{pmatrix} F_1(k) & & 0 \\ & \ddots & \\ 0 & & F_n(k) \end{pmatrix}, \quad F_i = \begin{pmatrix} \cos(\omega_i(k)) & \sin(\omega_i(k)) \\ -\sin(\omega_i(k)) & \cos(\omega_i(k)) \end{pmatrix} \quad (29)$$

such that the state may be propagated through one discrete time step:

$$\theta(k+1) = F(k+1, k)\theta(k) \quad (30)$$

The one-step ahead prediction of the sinusoidal portion of the signal $y(k)$ is then:

$$s(k) = J^T F(k, k-1) \theta(k-1) \quad (31)$$

In least squares fashion, a quadratic error cost function is employed:

$$V = \sum_{k=1}^L \lambda(k)^{j-k} [y(k) - s(k)]^2 = \sum_{k=1}^L \lambda(k)^{j-k} [y(k) - J^T F^{k-j} \theta(j)]^2 \quad (32)$$

which is equivalent to the square of the measurement noise, ν^2 . The forgetting factor $\lambda(k)$ is introduced to discount old measurements, and is updated by:

$$\lambda(k) = \lambda_0 \lambda(k-1) + (1 - \lambda_0) \lambda_\infty \quad (33)$$

The following state estimate is reached by minimizing the above cost function:

$$\hat{\theta}(k) = F \hat{\theta}(k-1) + K(k) [y(k) - \hat{y}(k|k-1)] \quad (34)$$

where the gain $K(k)$ is given as:

$$K(k) = G(k)^{-1} J, \quad G(k) = J J^T + \lambda(k) F(k) G(k-1) F^T \quad (35)$$

and $\hat{y}(k|k-1)$ is a one-step ahead prediction of $y(k)$ using Equation 31.

Estimates of the amplitude, frequency, and phase offset are all derived from the state estimate. To be precise, the amplitude estimate of the i^{th} sinusoidal component is obtained by the relationship:

$$\hat{A}_i(k) = \|\theta_i(k)\| = \sqrt{\hat{\theta}_{is}^2(k) + \hat{\theta}_{ic}^2(k)} \quad (36)$$

where the *is* and *ic* subscripts respectively denote the *sin* and *cos* parts of the θ_i element of the state vector. The argument estimate of the sinusoidal component is determined by:

$$\hat{\eta}_i(k) \equiv \hat{\omega}_i(k)k + \hat{\phi}_i = \arctan \left(\frac{\hat{\theta}_{is}(k)}{\hat{\theta}_{ic}(k)} \right) \quad (37)$$

The difference between two consecutive argument estimates is equivalent to the frequency averaged over the time differential:

$$\delta \hat{\eta}_i(k) = \hat{\eta}_i(k) - \hat{\eta}_i(k-1) = \bar{\omega}_i(k) \quad (38)$$

The frequency estimate is then assembled using the recursion formula:

$$\hat{\omega}_i(k) = \mu(k) \hat{\omega}_i(k-1) + (1 - \mu(k)) \delta \hat{\eta}_i(k) \quad (39)$$

where $\mu(k)$ is a convergence factor incorporated to smooth the frequency estimates. It is also updated in the same manner as $\lambda(k)$. The phase offset estimate is deduced from using the argument and frequency estimates and: $\hat{\phi}_i = \hat{\eta}_i(k) - \hat{\omega}_i(k)k$.

The ALS approach described here is simple yet quite powerful. Similar to the IIR ANF, the estimates approach the Cramer-Rao bound for accuracy. As input, the algorithm

requires the following: sampling frequency, the number of signals to estimate parameters for, forgetting factor values, and the data sequence. No initial parameter estimates are needed.

7.0 DATA PROCESSING COMPARISON RESULTS

This section presents the results from processing the simulated baseband signal data for the CGADS receiver. Compared are the basic FFT method as well as the AR-LS and ANF-ALS methods proposed here. Frequency and electrical phase accuracy results are provided for SNR values from 20-35 dB, baseband frequencies from 500-600 Hz, A/D quantization levels from 2-8 bits, and Doppler rates from 10-100 Hz/s. The results are based on the simplified signal model shown in Section 2.2 with parameter values given in Table 1 used unless otherwise noted.

Table 1: Nominal parameters for signal processing analysis.

Antenna A Initial Phase	30 degrees
Phase Difference B - A	20 degrees
Baseband Frequency	500 Hz
Doppler Rate	100 Hz/s
SNR	20 dB
Quantizer Resolution	1/16 of full scale

In each of the frequency and phase error graphs to follow, the solid line (—) corresponds to the FFT estimate; the dashed line (- -) corresponds to the AR-LS estimate; and the dash-dot line (-.-) corresponds to the ANF-ALS estimate.

7.1 THERMAL NOISE EFFECTS

Using the SNR based thermal noise model presented in Section 2.2, FFT results were generated for signal strengths of 20 and 35 dB, with and without the Hanning window applied to the data. A series of 100 runs were executed and then combined to average the effects of the random noise present in the thermal phase error. The results are summarized in Table 2, where $\text{RMS}(\hat{f} - f_{true})$ represents the RMS of the error in the frequency estimates, and $\text{RMS}(\hat{\phi} - \phi_{true})$ represents the RMS of the error in the phase estimates.

Table 2: Effect of Hanning window on FFT performance in the presence of thermal noise .

SNR	Hanning	$\text{RMS}(\hat{f} - f_{true})$ [Hz]	$\text{RMS}(\hat{\phi} - \phi_{true})$ [deg]
35	yes	4.98	0.118
35	no	4.98	0.121
20	yes	5.00	0.119
20	no	5.00	0.125

The table shows that there is only a minimal improvement due to the Hanning window. On average, the nominal signal level of 20 dB produces frequency errors of 5 Hz and phase errors of 0.1 degrees due to thermal noise.

Using the SNR based thermal noise model presented in Section 2.2, frequency and phase results were generated for signal strengths from 20-30 dB. The errors for the three data processing methods are shown in Figure 6. The frequency error for the FFT method is constant at 5 Hz due to the frequency bin width of 10 Hz and the average frequency of 505 Hz during the 0.1 second interval. The AR and ANF methods produce less than 1 Hz of error for all SNR values considered. The phase errors for all approaches were within 0.5 degrees, with the FFT and AR-LS methods producing errors within 0.2 degrees for all SNR values considered. As will be shown subsequently, the phase errors are dominated by Doppler rate effects.

7.2 BASEBAND FREQUENCY

With a sample frequency of 2560 Hz and a batch of 256 samples, the FFT frequency spacing is 10 Hz. Errors in the frequency and phase estimates due to the alignment of the actual signal frequency within the bin were investigated by varying the baseband (or center) frequency from 500 to 600 Hz in 1 Hz increments. Figure 7 illustrates the results. As expected, the FFT method shows a frequency error due to the bin width. Frequency errors in the other approaches are negligible. Again the phase errors for the FFT and AR-LS are mostly within 0.2 degrees. The ANF-ALS approach produced higher phase errors, in some cases as much as 1 deg. The accuracies of the AR and ANF-ALS techniques are not dependent upon the sampling frequency being a multiple of the signal frequency.

7.3 QUANTIZATION LEVEL

A range of quantization levels from 2-256 for the full scale of the A/D converter were considered, where a value of 2 corresponds to a 1-bit A/D and 256 corresponds to an 8-bit A/D. The results are shown in Figure 8. Frequency errors were not affected by changes in the number of quantization levels. Phase errors larger than 1 degree were observed for the 1-bit A/D converter, but the phase error was reduced to within 0.2 degrees for all methods with a 5 bit A/D converter. No additional improvements were observed by going beyond 6 bits (64 levels).

7.4 DOPPLER RATES

The largest effect on performance was observed by varying the Doppler rate of change from 10 Hz/s to 100 Hz/s in 10 Hz/s increments, as illustrated in Figure 9. On the frequency graph the AR-LS and ANF methods show the expected high performance. The FFT method shows a linearly changing error which takes a jump as the mean frequency within the 0.1 sec data interval shifts the result from one Doppler bin to the next. The phase data estimates for both FFT and AR-LS methods show a peak error of almost 0.3 degrees corresponding to a Doppler rate of change of 70 Hz/s. It is not obvious why this particular value had the worst results. The ANF-ALS method is the least effective producing errors of more than 1 degree.

8.0 SUMMARY AND RECOMMENDATIONS

A preliminary investigation of the effects of multipath on the codeless receiver processing was completed. Effects of noise, quantization, baseband frequency, and Doppler rates on FFT frequency and phase estimates were also presented. Two alternative algorithms, the AR-LS and combined ANF-ALS approaches were described. The AR-LS provided consistently improved performance over the standard FFT algorithms using the simplified simulation models. The ANF-ALS approach worked well for frequency identification but did not provide highly accurate phase values. Despite this, the method should not be completely eliminated from consideration because it has the advantage that it is implemented recursively (rather than on a batch of data) and can be readily applied to situations where frequency and phase values are changing.

The study results presented here do not take into account many receiver specifics including effects of filters, limiters and other hardware devices. Furthermore, the alternative algorithms proposed may require signal processing capabilities which are not designed into the breadboard CGADS receiver. To truly confirm the performance predicted above, and to further investigate the validity of the alternative algorithms, experimental data from a prototype CGADS receiver would be required.

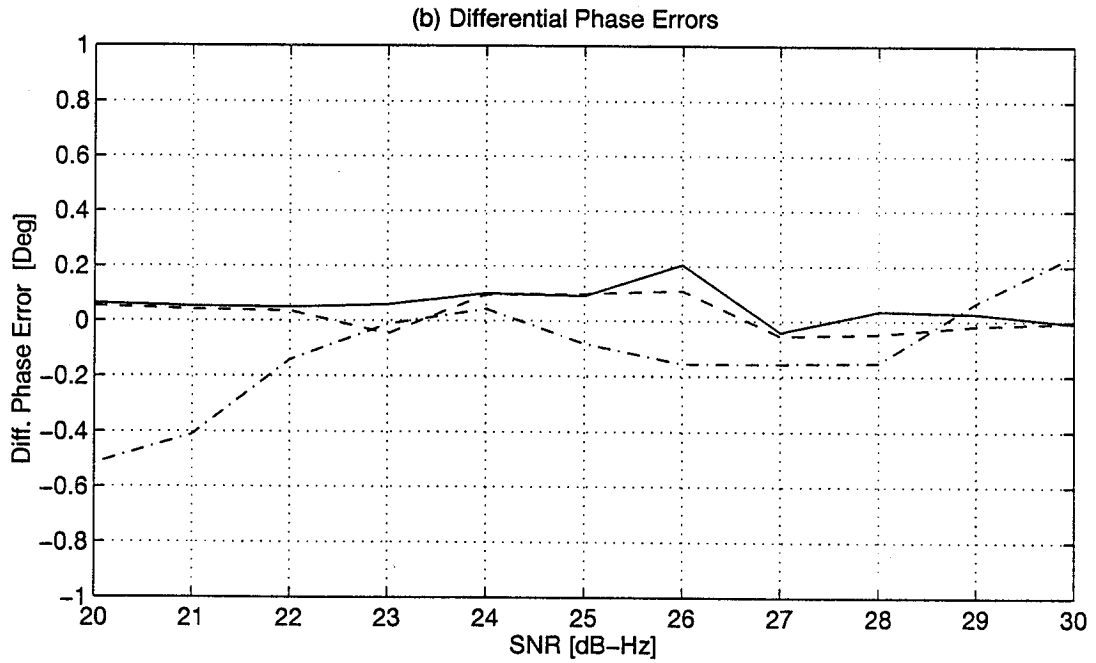
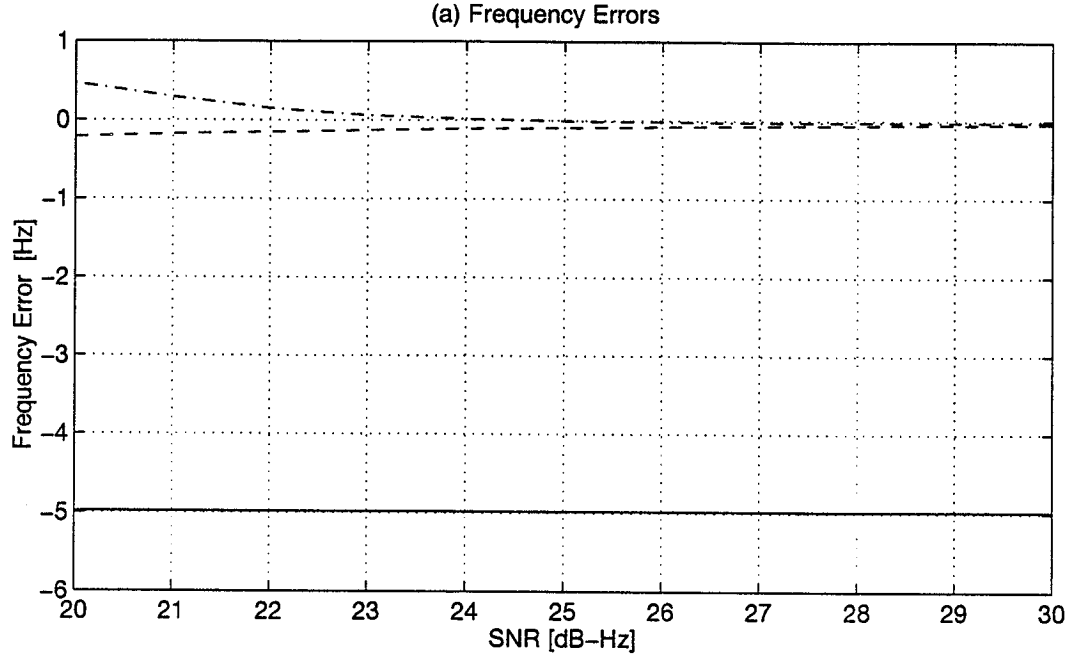


Figure 6: FFT, AR-LS, and ANF-ALS results from varying thermal noise from 20 to 30 dB: (a) error in frequency estimates, (b) error in phase estimates.

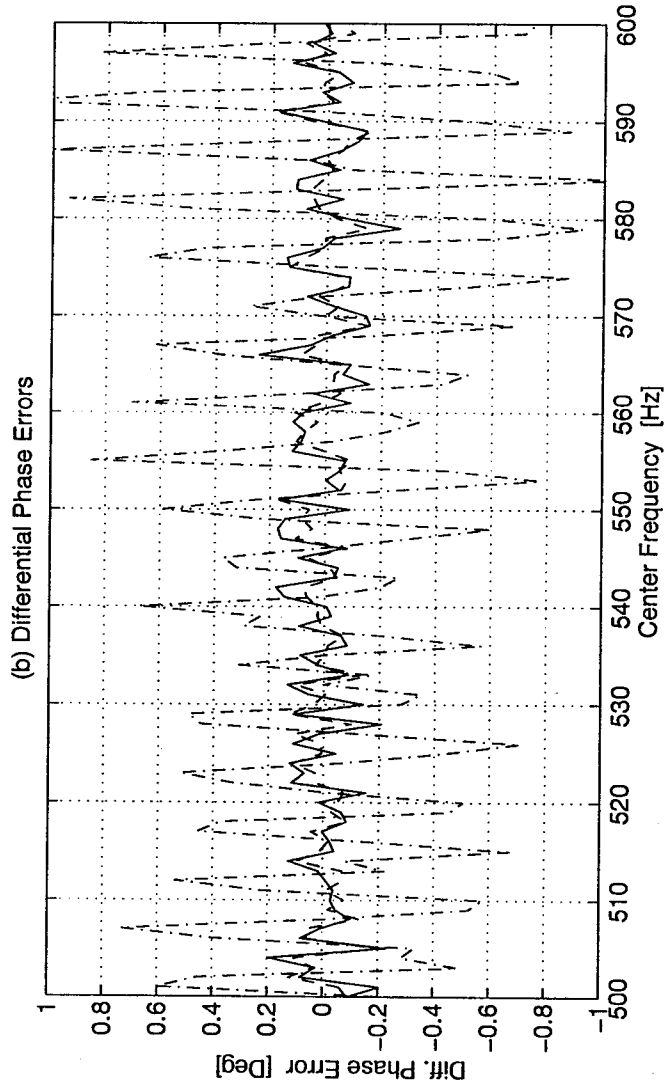
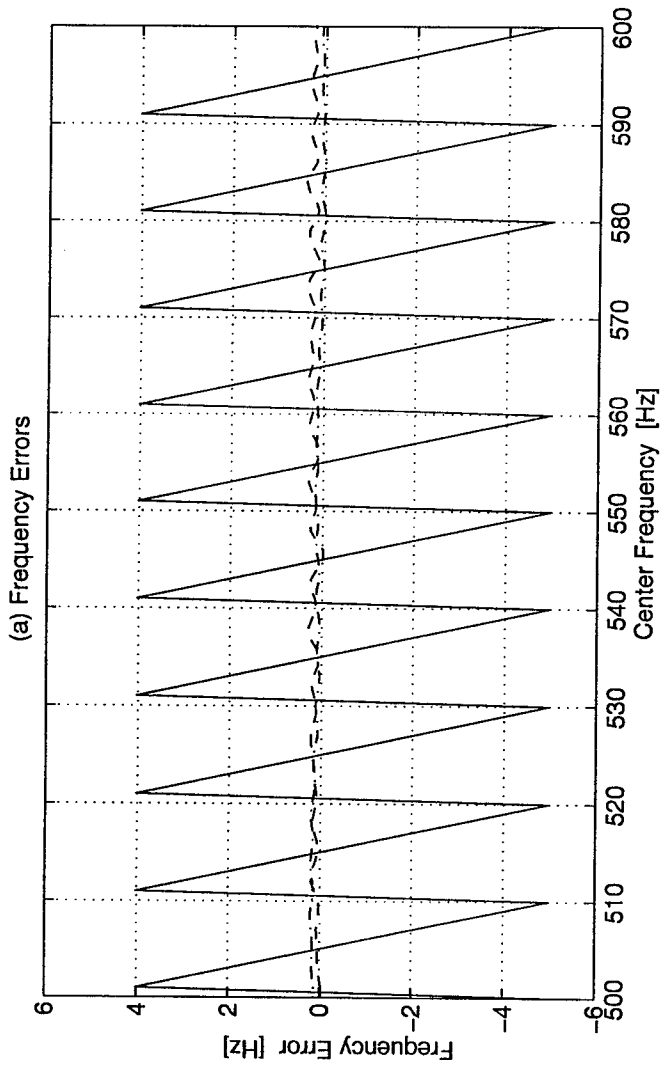


Figure 7: FFT, AR-LS, and ANF-ALS results from varying baseband/center frequency from 500 to 600 Hz: (a) error in frequency estimates, (b) error in phase estimates.

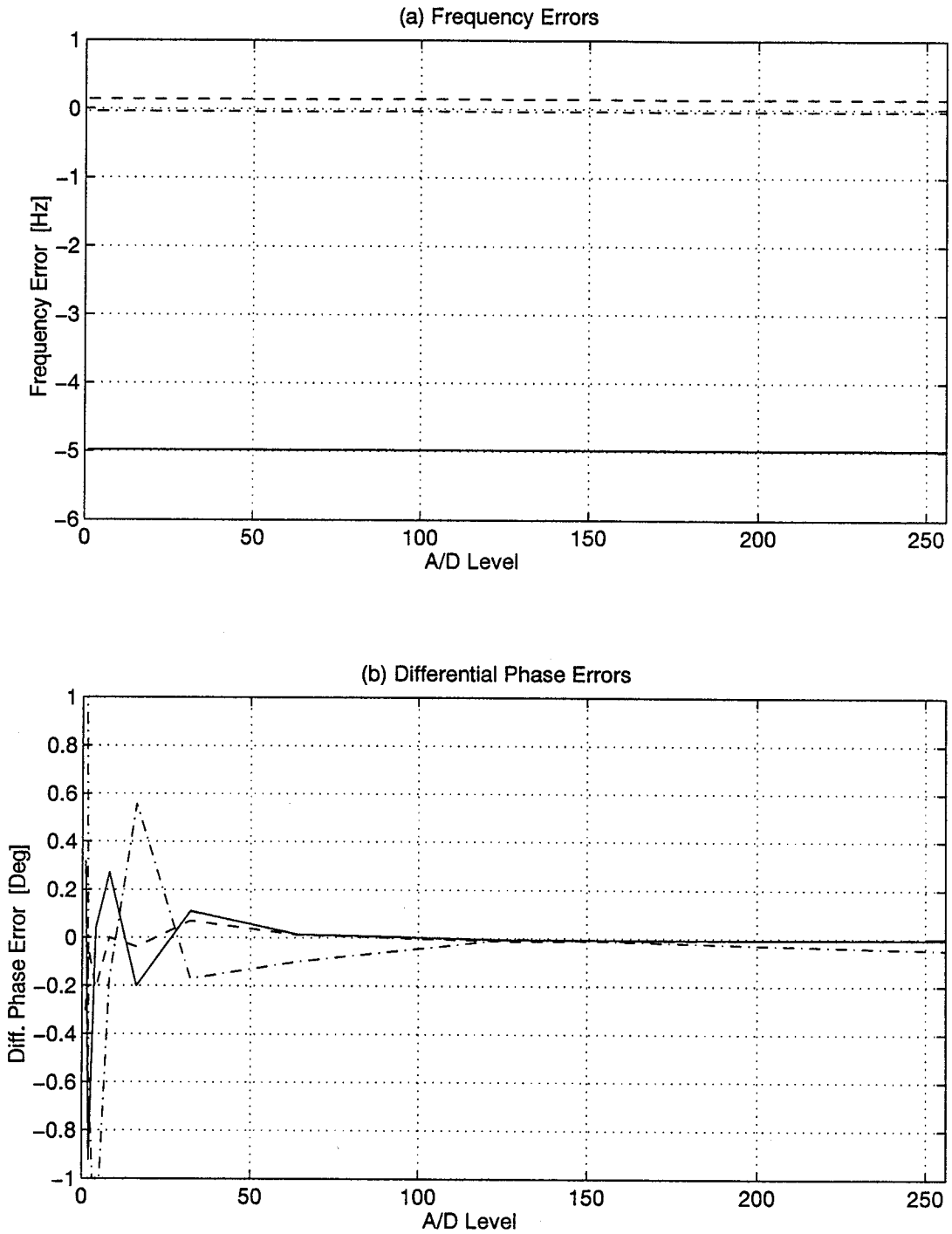


Figure 8: FFT, AR-LS, and ANF-ALS results from varying A/D quantization level from 2 to 256 full scale: (a) error in frequency estimates, (b) error in phase estimates.

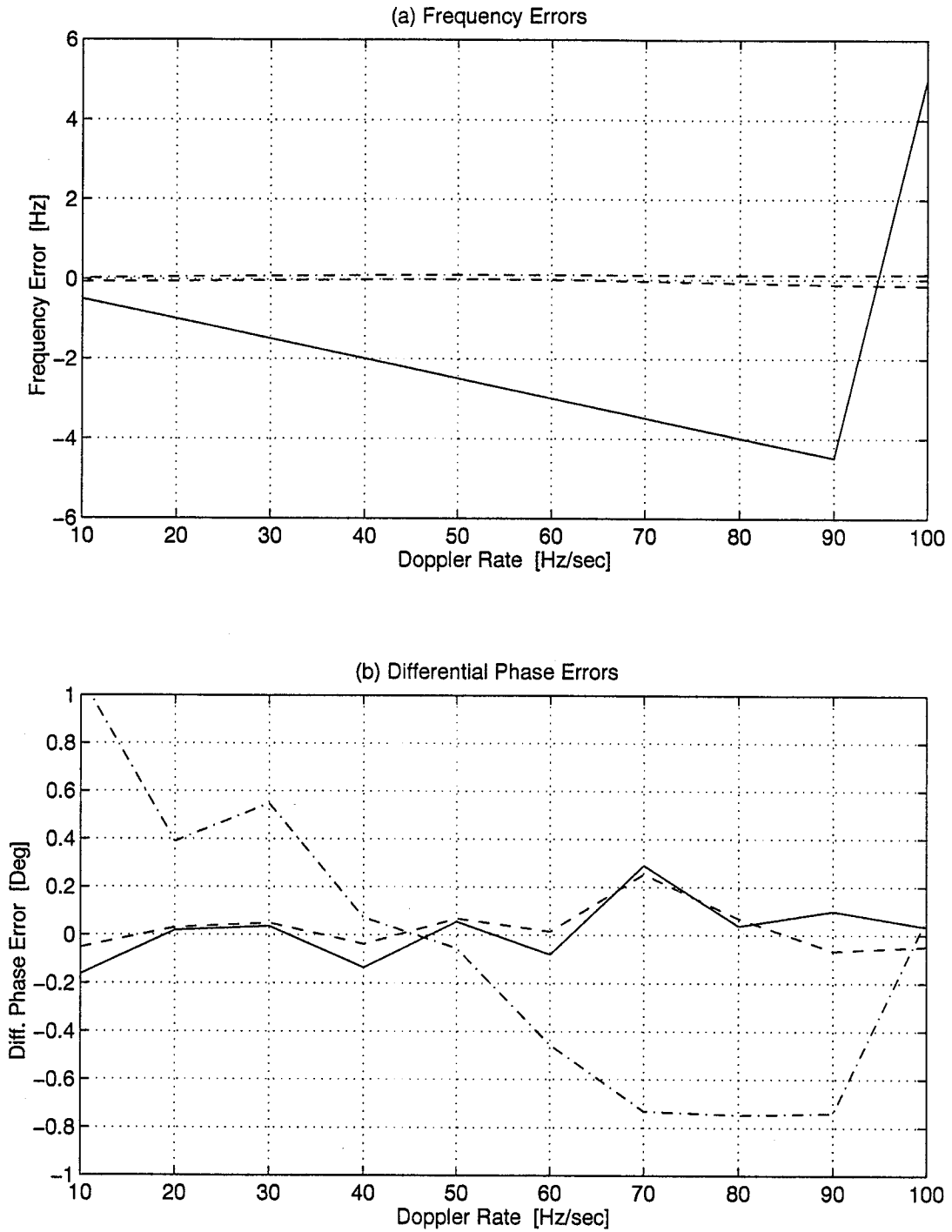


Figure 9: FFT, AR-LS, and ANF-ALS results from varying Doppler rate from 10 to 100 Hz/s: (a) error in frequency estimates, (b) error in phase estimates.

REFERENCES

- [1] Chicharo, J.F., "High Resolution Spectral Estimation Using a Specially Constrained Adaptive Notch Filter," *International Journal of Electronics*, Vol. 72, No. 1, pp. 57-66, 1992.
- [2] Kay, Steven M., *Modern Spectral Estimation Theory and Application*, Prentice Hall, 1988.
- [3] Ljung, L. and T. Söderström, *Theory and Practice of Recursive Identification*, The MIT Press, Cambridge, MA, 1985.
- [4] Nehorai, A., "A Minimal Parameter Adaptive Notch Filter With Constrained Poles and Zeros," *IEEE Transactions on Acoustics, Speech, and Signal Processing*, Vol. ASSP-33, No. 4, pp. 983-996, Aug., 1985.
- [5] Nehorai, A. and B. Porat, "Adaptive Comb Filtering for Harmonic Signal Enhancement," *IEEE Transactions on Acoustics, Speech, and Signal Processing*, Vol. ASSP-34, No. 5, pp. 1124-1138, Oct., 1986.